arXiv:astro-ph/0010652v1 31 Oct 2000

# Measurement of the Cosmic Ray Energy Spectrum and Composition from $10^{17}$ to $10^{18.3}$ eV Using a Hybrid Fluorescence Technique

T.Abu-Zayyad[1], K.Belov[1], D.J.Bird[5], J.Boyer[4], Z.Cao[1], M.Catanese[3], G.F.Chen[1], R.W.Clay[5], C.E.Covault[2], H.Y.Dai[1], B.R.Dawson[5], J.W.Elbert[1], B.E.Fick[2], L.F.Fortson[2a], J.W.Fowler[2], K.G.Gibbs[2], M.A.K.Glasmacher[7], K.D.Green[2], Y.Ho[10], A.Huang[1] , C.C.Jui[1], M.J.Kidd[6], D.B.Kieda[1], B.C.Knapp[4], S.Ko[1], C.G.Larsen[1], W.Lee[10], E.C.Loh[1], E.J.Mannel[4], J.Matthews[9], J.N.Matthews[1] , B.J.Newport[2], D.F.Nitz[8], R.A.Ong[2], K.M.Simpson[5], J.D.Smith[1], D.Sinclair[6], P.Sokolsky[1], P.Sommers[1], C.Song[10], J.K.K.Tang[1], S.B.Thomas[1], J.C.van der Velde[7], L.R.Wiencke[1], C.R.Wilkinson[5], S.Yoshida[1] and X.Z.Zhang[10]

[1] *High Energy Astrophysics Institute,*
*University of Utah,*
*Salt Lake City UT 8 4112 USA*

[2] *Enrico Fermi Institute,*
*University of Chicago,*
*Chicago IL 60637 USA*

[3] *Smithsonian Astrophys. Obs.,*
*Cambridge MA 02138 USA*

[4] *Nevis Laboratory, Columbia University,*
*Irvington NY 10533 USA*

[5] *University of Adelaide,*
*Adelaide S.A. 5005 Australia*

[6] *University of Illinois at Champaign-Urbana,*
*Urbana IL 61801 USA*

[7] *University of Michigan,*
*Ann Arbor MI 48109 USA*

[8] *Dept. of Physics,*
*Michigan Technological University,*

*Houghton, MI 49931 USA*

[9] *Dept. of Physics and Astronomy,*

*Louisiana State University,*

*Baton Rouge LA 70803 and*

*Dept. of Physics, Southern University,*

*Baton Rouge LA 70801 USA*

[10] *Dept. of Phys., Columbia University,*

*New York NY 10027 USA*

[a] *joint appt. with The Adler Planetarium and Astronomy Museum,*

*Astronomy Dept., Chicago IL 60605 USA*

(Dated: February 1, 2008)

## Abstract

We study the spectrum and average mass composition of cosmic rays with primary energies between $10^{17}$eV and $10^{18}$eV using a hybrid detector consisting of the High Resolution Fly's Eye (HiRes) prototype and the MIA muon array. Measurements have been made of the change in the depth of shower maximum as a function of energy. A complete Monte Carlo simulation of the detector response and comparisons with shower simulations leads to the conclusion that the cosmic ray intensity is changing from a heavier to a lighter composition in this energy range. The spectrum is consistent with earlier Fly's Eye measurements and supports the previously found steepening near $4 \times 10^{17}$eV .

## I. INTRODUCTION

The source of cosmic rays with particle energies above $10^{14}$ eV is still unknown. Models of origin, acceleration, and propagation must be evaluated in light of the observed energy spectrum and chemical composition of the cosmic rays. Several experiments have attempted to determine the mean cosmic ray composition through the "knee" region of the spectrum, up to $3 \times 10^{16}$eV[1]. While the results are not in complete agreement, there is some consensus for a composition becoming heavier at energies above the knee, a result consistent with charge-dependent acceleration theories or rigidity-dependent escape models.

In the region above the knee, the Fly's Eye experiment has reported a changing composition from a heavy mix around $10^{17}$eV to a proton dominated flux around $10^{19}$eV [2]. This result makes this particular energy region much more interesting than the expectation from a naive rigidity model. This changing composition may imply that there may be multiple sources of cosmic rays. The AGASA experiment shows broad agreement with this trend if the data are interpreted using the same hadronic interaction model as used in the Fly's Eye analysis [3, 4].

The recently reported HiRes/MIA[5] hybrid observation on the cosmic ray composition in a narrower energy region, $10^{17} \sim 10^{18}$ eV, shows a general agreement with Fly's Eye experimental result. The new result gives a somewhat more rapid change in the composition. The reliability of these experimental results depends on how well we understand the development of all components of extensive air showers (EAS) produced by cosmic rays, how well we understand the response of our detector to the EAS, and how well we have done in the EAS reconstruction. In this paper, we address all those issues in detail. We start with a general description of the techniques of cosmic ray composition measurement in the high energy region.

### A. Existing Techniques of Compostion Measurement above $10^{17}$eV

The Fly's Eye and AGASA experiments use different techniques to study composition. The Fly's Eye experiment technique is based on the assumption that the speed of the development of EAS depends on the mass of the primary particle: a heavier nucleus induces earlier EAS development in the atmosphere. The rapid break-up of a heavy nucleus at

the early stage of the cascade in the air leads to an effectively higher multiplicity than that produced by a light nucleus or a proton at the same depth in the atmosphere. The consequence is that the EAS is built up by a superposition of smaller subshowers induced by nuclear fragments. In this case, since the subshowers have lower energies, the EAS will have a shower maximum higher in the atmosphere than in the case for a proton primary. The Fly's Eye experiment is designed to measure the size, or total number of charged particles, of an EAS as a function of atmospheric depth. It is thus an ideal detector to measure the depth of maxima of showers directly.

In practice, the intrinsic fluctuations in the depth of shower maximum and the detector resolution effects imply that one can not directly resolve the type of primary nucleus on an event by event basis. What one can do is to extract an average EAS primary composition by comparing the data to a Monte Carlo simulation with a given primary composition. Since the shower development is somewhat dependent on the choice of a hadronic model, this method leads to results which have some model dependence.

The other method for studying composition depends on the assumption that the muon content of EAS produced by a superposition of sub-showers ( as in the case of heavy nuclei ) is larger than those with fewer sub-showers. This is due to the fact that the dissociation of a heavy nucleus produces a relatively higher multiplicity in its interaction with atmospheric nuclei. The resultant sharing of the primary energy between the nuclear fragments make the secondary pions less energetic. As a consequence, those pions have a greater decay probability into muons than those produced by a lighter nucleus in the early stage of shower development. This leads to a difference in the muon content between the EAS's induced by heavier and lighter nuclei, e.g. iron and protons. This difference shrinks with energy because the available path for the decay of the high energy pions decreases as the shower develops deeper in the atmosphere. According to the simulations the difference is still resolvable in the energy region $10^{17} \sim 10^{18}$ eV.

In principle , one can obtain the information about the composition of the primary particle by either measuring the total number of muons in EAS or a local density of shower muons at a specific distance to the core of the shower. However, as in the case of the previous method, the fluctuations are large compared with the separation between the different types of EAS, so that the resolvability is not strong. The hadronic model dependence of the predicted $\mu$-content from a particular composition is also significant for this method.

### B. Advantages and Challenges for the HiRes/MIA Experiment

The HiRes/MIA hybrid experiment is designed to combine the two methods together using two independently developed co-sited experiments. The two experiments share a trigger to simultaneously record both the longitudinal development information and the EAS muon density. This results in a unique data set useful for the investigation of cosmic ray composition. Results on comparison of the flourescence and muon methods have previously been published[5]. In this paper, we use the MIA array to improve the geometrical reconstruction and concentrate on the fluorescence technique for composition and spectrum studies.

The hybrid timing information enhances the accuracy in the determination of the geometry of the EAS. This accurate shower geometry plays a crucial role in the subtraction of the Cerenkov light component of the EAS and in the corrections for detector acceptance. These turn out to be the two key issues in the shower longitudinal development profile determination. This profile provides directly the size at shower maximum and its location while the integral of the profile yields the shower energy. The improvement in shower geometry determination is the main advantage of a hybrid experiment. The other advantage resulting from the coincident measurement with the surface muon array is the existence of a fully efficient triggering region in the central detector volume. This is very helpful for the cosmic ray energy spectrum measurement.

One of the challenges for this experiment is that the two devices are separated by only 3.3 km. Because the MIA detector can not be triggered by remote showers, most of the triggered events are located $\sim 4$ km away from HiRes detector. This short shower-detector distance gives rise to difficulties for reconstruction of those EAS's. The lateral distribution of shower electrons is no longer a negligible effect. The broadened source of light increases the uncertainty in the shower geometry determination and in the acceptance correction of the signals. The limited effective trigger area of MIA largely suppresses the aperture of HiRes detector. The energy coverage of our data is one decade of magnitude over 3 years of observation, much smaller than that from the Fly's Eye experiment. The geometry of the triggered events is such that the fraction of Cerenkov light is often large. This implies the need for tight criteria for event selection to reduce Cerenkov contamination, which in turn may cause a bias. We must search for a balance between the tightness of the selection criteria and the minimization of bias. We describe our resolution of these problems in the

following sections.

## II. HIRES AND CASA/MIA EXPERIMENTS AND HYBRID OBSERVATION

In this experiment, we use a hybrid detector consisting of the prototype High Resolution Fly's Eye (HiRes) air fluorescence detector and the Michigan Muon Array (MIA). The detectors are located in the western desert of Utah, USA at 112° W longitude and 40° N latitude. The HiRes detector is situated atop Little Granite Mountain at a vertical atmospheric depth of 860 g/cm$^2$. It overlooks the CASA-MIA arrays some 3.4 km to the northeast. The surface arrays are some 150 m below the fluorescence detector at an atmospheric depth of 870 g/cm$^2$.

### A. The HiRes Detector

The HiRes prototype has been described in detail elsewhere [6]. It views the night sky with an array of 14 optical reflecting telescopes. They image the EAS as it progresses through the detection volume from 3° to 70° in elevation, 64° in azimuthal angle at the top and 32° at the bottom of the field of view. Nitrogen fluorescence light (in the 300–400 nm band) is emitted at an atmospheric depth $X$ in proportion to the number of charged particles in the EAS at that depth, $S(X)$. The triggered tube directions and the time of arrival of light signals can be used to determine the shower-detector-plane and the tilt angle of the shower in this plane, denoted by $\psi$. Part of the shower development profile (at least 250 g/cm$^2$ long) can be mapped by measuring the light flux arriving at the detector. Assuming $S(X)$ to be the Gaisser-Hillas [7] shower developement function and correcting for Cerenkov light contamination and atmospheric scattering effects one can measure the primary particle energy $E$, and the depth, $X_{max}$, at which the shower reaches maximum size[8].

### B. The MIA Detector

The MIA detector [9], consisting of 16 patches formed with 64 scintillation counters each, covers about 370m $\times$ 370 m with the active area over 2500 m$^2$. The patches are buried about 3 m under the surface. The data acquisition system records the identity and firing time of

each counter participating in a given event. The EAS muon arrival times are measured with a precision of 4 ns and all hits occurring within 4 $\mu$s of the system trigger are recorded. The average efficiency of MIA counters for detecting minimum ionizing particles was 93% when they were buried, and the average threshold energy for vertical muons is about 850 MeV. The MIA detector determines the muon density via the number and pattern of hit counters observed in the shower [10].

### C. The Hybrid Trigger and Event Sample

The HiRes detector collects data on clear moonless nights. A focal plane camera, consisting of 16×16 photo-multiplier-tubes (PMT), is triggered if two of its 4×4 "sub-clusters" contain at least 3 fired tubes(two of them must be physically adjacent) in a 25 $\mu$s interval. Tubes trigger if the signal generates a voltage greater than a threshold, set at approximately 4 $\sigma$ above nightsky background noise. This yields a mirror trigger rate of about 30 to 120 per minute. Once a trigger is formed, HiRes sends a Xenon light flash to MIA as a confirming trigger for a coincident event.

MIA has a 100% duty cycle and a trigger rate of about 1.5Hz formed by requiring at least 6 patches fired ( with at least 3 hits found in each patch). However, a coincident event is not selected until either it is confirmed by a HiRes light flash communication signal if it is received within 50$\mu$s, or the event triggers CASA (a surface scintillation detector array for EAS electron observation[9]) simultaneously and is coincident with a HiRes event within ±3 ms according to the GPS clocks in each site. More details about the trigger formation and coincident event matching can be found in [11].

During the lifetime of this hybrid experiment between Aug. 23, 1993 and May. 24, 1996 the total coincident exposure time was 2878 hours corresponding to a duty cycle of 11.9%. 4034 coincident events were recorded. For events passing a set of coincidence assurance cuts the shower trajectory, including arrival direction and core location for each event, was obtained in an iterative procedure using the information from both HiRes and MIA [11]. 2491 events survive this reconstruction procedure. Further cuts are performed in order to maintain high resolutions in energy and shower maximum which are essential to the composition analysis. The criteria are based on a thorough Monte Carlo simulation of the detectors as described below. After quality cuts, 891 events are employed in this composition

study and energy spectrum measurement.

### D. Shower Geometry Determination

Accurate knowledge of the shower geometry is important in the reconstruction of the shower profile in the atmosphere. The first step is to use the pointing directions of triggered pixels in the HiRes detector to determine the shower-detector-plane. This is a simple linear fit weighted by the amount of light received by each tube. The shower-detector-plane is determined quite precisely because the HiRes detector records showers with an average of 36 triggered pixels and the quality cut ensures that the lengths of tracks is longer than 20°. The typical error in the horizontal position of the plane is about 0.1°, while the error in the tilt angle of the plane is somewhat larger. The overall error in the shower-detector-plane normal direction is about 0.7°.

Muon timing information from MIA plays a key role in the determination of geometric parameters in the shower-detector-plane, including the shower-detector distance and shower orientation, and in the improvement of the shower-detector-plane determination. The initial trial shower arrival direction is determined by fitting the muon arrival time with a flat shower front. Projecting this direction onto the shower-detector-plane yields the tilt angle of the shower, $\psi$, defined as the angle between the shower axis and the horizon in the shower-detector-plane.

Once $\psi$ is known, the light arrival time, $t_i$, on the $i$-th fired HiRes tube is fit to the timing formula

$$t_i = t_0 + \frac{R_p}{c}\mathrm{ctan}\frac{\chi_i + \psi}{2}, \tag{1}$$

in which $\chi_i$ refers to the elevation angle of the $i$-th fired tube. $t_0$ and $R_p$ are two parameters indicating the time as the shower front passes the detector and the perpendicular distance from the shower axis to the detector respectively, while $c$ refers to the speed of light( see the sketch in FIG. 1).

The core location can be derived by using the shower-detector-plane normal vector, $\psi$ and $R_p$. The shower front shape can now be more accurately represented as a cone with the delay parameter $\Delta = ar + br^2$, where $\Delta$ refers to the delay of a conical muon front relative to the original flat front at a perpendicular distance, $r$, to the shower axis. This procedure

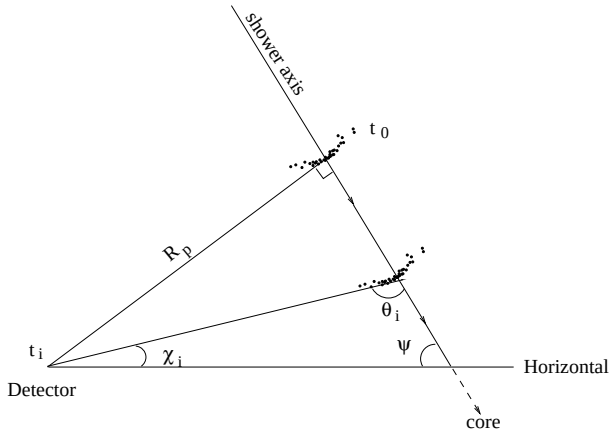


FIG. 1: Illustration of shower geometric parameters in the shower-detector-plane

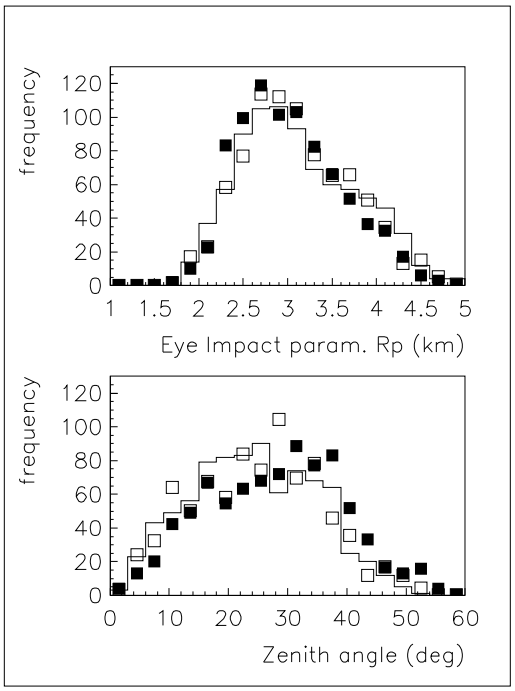


FIG. 2: $R_p$ and zenith angle distributions. Filled squares are Monte Carlo predictions for proton, open squares for Fe (see text in next section for details).

is iterated after additional corrections, including correction to the shower-detector-plane direction. This iteration stops when the difference between the core parameters is less than 10m. The details of this iterative procedure can be found in [11]. The distributions of those parameters are shown in FIG. 2 and FIG. 3.

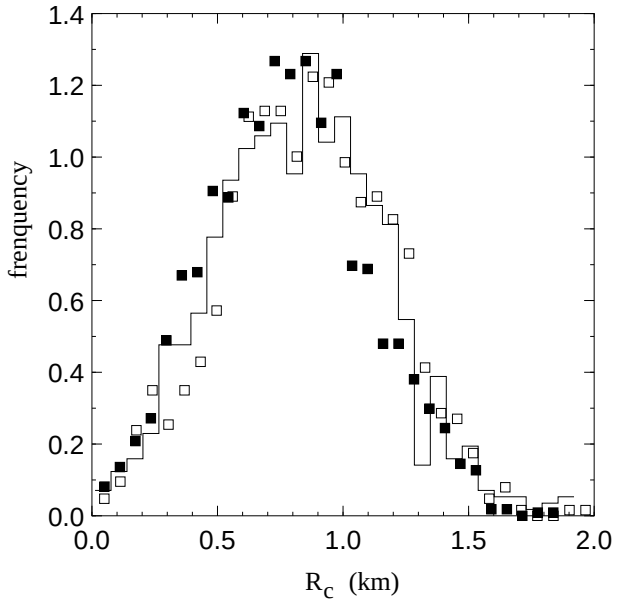


FIG. 3: Core location distribution with respect to the MIA center. Filled squares are Monte Carlo predictions for proton, open squares for Fe (see text in next section for details).

### E. Shower Longitudinal Development Reconstruction

The HiRes tube signal, consisting mainly of the fluorescence light produced by charged particles from the shower, can be used to reconstruct the shower development, i.e. to calculate the shower size at the corresponding depth in the atmosphere. For this purpose, the raw tube signal must be corrected for several effects.

If a triggered tube has a center that is not exactly in the shower-detector plane, its signal requires correction for a number of effects. These include the finite transverse width of the shower due to multiple scattering of shower electrons, the finite size of the optical spot on the face of the focal plane camera, the response function of the PMT cathode, gaps between the pixels, and the effective light collecting area of mirrors. All these effects can be taken into account by performing a "ray tracing" procedure, namely we trace the photons from the source direction, which can be wider than a line source due to the lateral distribution of shower electrons, all the way down to the face of the PMT via the spherical mirror surface. The response function of the PMT cathode is folded into the ray tracing. The pixel signals are then re-organized into a series of longitudinal "bin signals" with a 1° bin size along the shower axis. The signals are recalculated in units of "number of photon-electrons per unit angle along the track per unit collecting mirror area". Ref. [11] provides the details of this

correction and binning procedure for interested readers.

The fluorescence light yield (photons per meter ) of a single charged particle varies slightly with the atmospheric pressure and temperature and has an energy dependence given by the dE/dX energy loss curve[12]. These effects are taken into account in our shower reconstruction. The energy dependence of the fluorescence light yield is folded in by taking an average over the shower electrons at age $s$, defined as $3X/(X + 2X_{max})$, with an energy distribution of the shower electrons at age $s$ being extracted from the simulation results using the CORSIKA package[13, 14]. This energy distribution is consistent with measurements by Richardson [15] and a parameterization from Hillas [16].

In addition to the corrections associated with those issues, the Cerenkov light component of the bin signal must be subtracted as well, because only the pure fluorescence light is proportional to the size of shower at a given depth. This gives rise to some complications. First of all, the Cerenkov light component is composed of the Cerenkov light produced by the shower electrons directly illuminating the detector and the light scattered into the direction of the detector. Because the Cerenkov light is very forward along the direction of the electrons, the angular distribution of Cerenkov light in a shower is narrowly beamed and falls exponentially with the angular distance from the shower axis. The average angular scale has been measured to be $4.0 \pm 0.3^{\circ}$[1]. Therefore, when the shower points towards the detector, the estimate of the Cerenkov light becomes very sensitive to the geometry of shower. In this case, the signal is also dominated by direct Cerenkov light. We avoid this sort of events in this analysis by a cut on the minimal viewing angle from the detector to the track, illustrated as the angle $\theta$ in FIG. 1.

The scattered Cerenkov light, which we still have to deal with, includes components due to the Rayleigh scattering from the atmospheric molecules and Mie scattering from aerosols. Rayleigh scattering is well understood in terms of the distribution of scattering centers and their fluctuations, angular distribution of light, frequency response and the overall extinction length for ultraviolet (UV) light. This scattering is used to estimate the attenuation of Cerenkov light along the shower, how much of this light is scattered into the PMT direction, and the attenuation of the light during the propagation from the source to the detector.

The scattering of UV light by aerosols is more uncertain. The distribution of aerosols depends on weather conditions. Because of the variation in the size distribution of aerosols,

the scattering phase function can vary. There are several models for this function which lead to different estimates of the amount of scattered light. We use the "standard desert aerosol model" with an exponential increase of the aerosol extinction length with height above a mixing layer of height $h_m$ below which the aerosol extinction length is constant. The change in extinction length with height above this is governed by a "scale height" parameter $h_s$ while below $h_m$, the extinction length is given by the "horizontal attenuation length", $\lambda_a$. We monitor the aerosol variation by the use of several Xenon flashers which shoot light pulses at different angles into the atmosphere at different distances to the detector. By detecting the scattered light from these flashers with the HiRes detector, we monitor the variation of aerosols[17] and partially constrain the range of those parameters. This will be discussed further in Sec. IV.

After subtracting the Cerenkov light components, the bin signals, now proportional to the size of the shower, are fit to a function describing the longitudinal development of EAS suggested by Gaisser and Hillas[7], (G-H function):

$$N(X) = N_{max} \left( \frac{X - X_0}{X_{max} - X_0} \right)^{(X_{max}-X_0)/\lambda} e^{(X_{max}-X)/\lambda}, \tag{2}$$

in which $N$ and $N_{max}$ refer to the size of the shower and its maximum, $X$ represents the atmospheric depth where the shower front passes the specific angular bin, and $X_0$ and $X_{max}$ the depths where the shower starts and reaches its maximum, respectively. The depth $X$ is calculated based on the shower geometric parameters and the pointing directions of each effective angular bin. The choice of this EAS longitudinal development curve has recently been experimentally confirmed [18] as accurate based on the same data set. The G-H function is one of the best parameterizations of longitudinal development according to this study.

An example of shower reconstruction is shown in FIG. 4. In a), the four components of light contributing to the best fit results are plotted: fluorescence light (thick solid line), direct Cerenkov light (thin solid line), Cerenkov light from Rayleigh scattering(dotted line) and Cerenkov light through aerosol scattering (dashed line). In b), we show the fit of the sum of all the components to the bin signals(dots). This shower reaches its maximum size of $1.6\times10^8$ at a depth of 630 g/cm$^2$. Note that the parameter $X_0$ is the point at which size $N = 0$ according to (2). We are not sensitive to light from early shower development and we fix $X_0$ at -20 g/cm$^2$ in our fitting procedure. The justification for this will be given below.

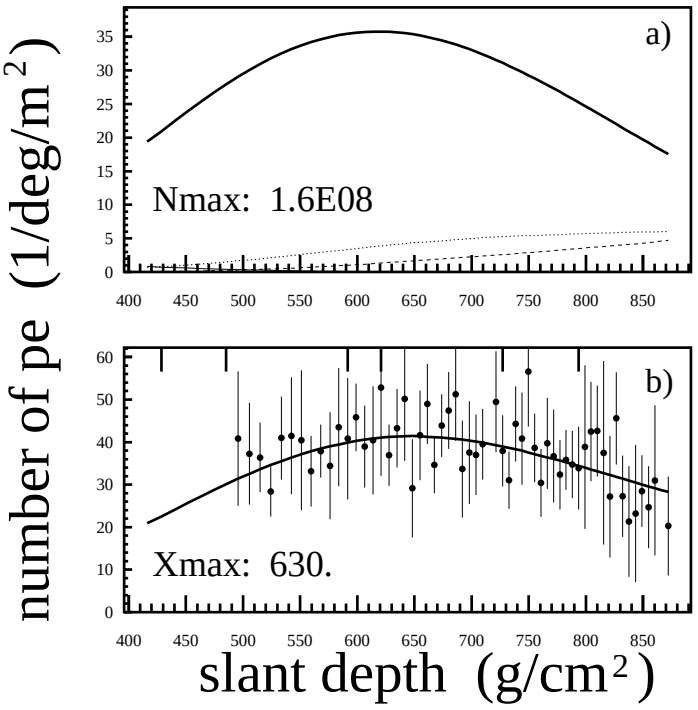


FIG. 4: A typical event. See the text for details.

### F. Shower Energy Determination

Once we know the longitudinal development profile of an EAS, we can integrate over its depth to calculate the total path length of all shower charged particles and calculate the total deposited energy $E_{e.m.}$ by the charged particles in this shower, i.e.,

$$E_{e.m.} = \frac{E_c}{L_0} \int N(X) dX, \tag{3}$$

where the critical energy and the radiation length of electrons in air are $E_c$ and $L_0$, respectively. A recent study[14] based on the Monte Carlo simulation package CORSIKA verifies this formula and re-evaluates the constant $E_c/L_0$ as 2.19. Since some of the primary energy is carried away by neutrinos and muons penetrating the ground, a correction for this effect must be applied. In that study, the authors establish a new empirical formula for the converting $E_{e.m.}$ into total energy of the shower, $E_0$. It reads

$$E_0 = \frac{E_{e.m.}}{A - B E_{e.m.}^{\kappa}} \tag{4}$$

where the parameter $A = 0.959 \pm 0.003$, $B = 0.082 \pm 0.003$ and $\kappa = -0.150 \pm 0.006$. These parameters are determined by taking an average between proton and iron initiated showers,

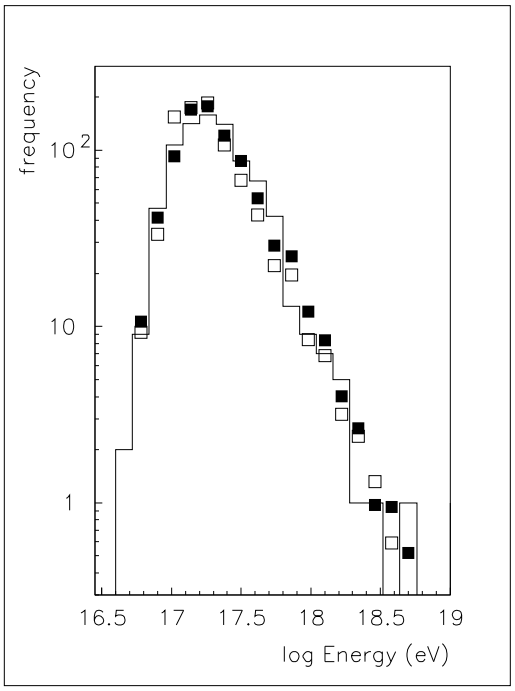


FIG. 5: Energy distribution. The histogram represents the data and the dots represent simulations, see text in Section IV for details.

since it is impossible to know the primary particle mass in advance of the reconstruction. This causes a systematic uncertainty in $E_0$ of less than 10%.

The energy distribution of our data set is displayed in FIG. 5. The vertical axis represents the number of events within a bin of $log_{10}$E. The figure shows that the threshold of our detector is about $5\times10^{16}$ eV. The hybrid detector approaches a fully efficient operation above $4\times10^{17}$ eV.

## III. MONTE CARLO STUDY OF DETECTOR RESOLUTIONS

In order to test this complex EAS reconstruction procedure and evaluate the resolution in shower geometry, shower depth of maximum and energy based on this reconstruction scheme, we have developed a Monte Carlo code to simulate the EAS shower and detector. We have made this as realistic as possible both for shower development in the atmosphere and for the response of our detector to the shower. In this section, we will address how this event generator is driven with a full Monte Carlo simulation of EAS, how the production and propagation of light through the atmosphere is treated, how the acceptance and response

of the detector to the light is simulated, and what the final resolution functions and their relationship with the event quality cuts are.

### A. Shower Generation: CORSIKA Package and Hadronic Interaction Models

The driver of the shower simulation is a series of parameterizations of the results from a full EAS simulation using the CORSIKA package[13]. This is one of the most modern and complete simulation codes for EAS development. It traces shower particles from very high energy at top of the atmosphere down to the threshold energy of 100 keV. A "thinning" technique is used in the simulation to reduce the size of the calculation. Only one secondary particle is traced if the interaction energy falls below the thinning threshold, e.g. $10^{-5}$ of the shower total energy. A weight is assigned to this traced particle to represent those not being traced. Depending on the degree of realism in the fluctuations that is required, the user can set an appropriate thinning threshold if the CPU time limit allows. Another advantage of the CORSIKA code is that the user can switch between several optional hadronic interaction models. The authors have made efforts to test the program for primary particle energies up to $10^{16}$ eV, but do not claim reliability for energies higher than $10^{17}$ eV. However, it is one of the best EAS models currently available. Low energy shower particles, down to the tens of keV level, are treated carefully by employing the well known EGS package [19] etc.

In our simulation with CORSIKA Ver. 5.624, the thinning threshold is set to be $10^{-5}$ of the shower energy and the QGSJET[20] and SIBYLL[21] hadronic interaction models are selected. The number of EAS electrons as a function of depth and EAS muon information, including arrival direction, time and energy for every muon above $870/\cos\theta$ MeV at 870 g/cm$^2$, are recorded. We simulated 500 events for each of the 5×4 grid points in energy from $3\times10^{16}$ eV to $5\times10^{18}$ eV and zenith angle from 0° to 60°. The same number of events were generated for proton and iron induced showers and under different hadronic interaction model assumptions.

### B. Shower Longitudinal Development Profile Parameterization

Based on this large simulated event data set, we parameterized all the distributions of EAS parameters such as the first interaction depth $X_1$, shower decay constant $\lambda$, shower maximum

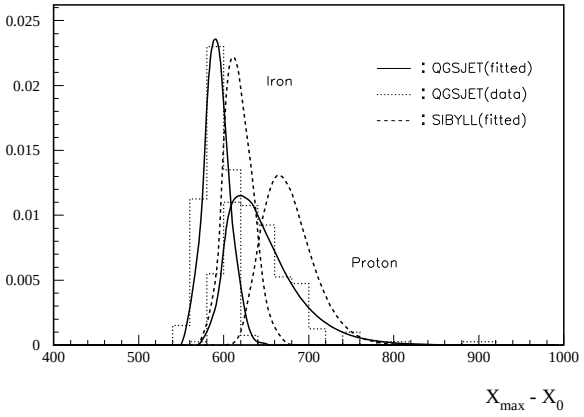


FIG. 6: The fluctuation of $X_{max}$ and its parameterization at $2 \times 10^{17}$ eV.

$N_{max}$, its position in depth $X_{max}$, and the correlations between them. As an example, the $X_{max}$-distribution is shown in FIG. 6. It is clear that the proton induced showers possess larger fluctuation in $X_{max}$ than iron initiated ones. Though they overlap each other, the means for each distribution are about 100 gm/cm$^2$ apart, which is resolvable if sufficient statistics are available. The model dependence appears to be significant, but is smaller than the proton-iron separation. The comparison between the histogram for simulated data and curves for parametrized results shows that the parameterization faithfully represents the fluctuation in $X_{max}$. A similar situation is found for the other parameters. Among the parameters, we find that $\lambda$ and $N_{max}$ are correlated and we put this correlation into our generator.

We find that the parameter $X_0$ is quite insensitive to the type of primary particle and energy if we use the G-H function (2) to fit the longitudinal development of simulated showers. The fitting quality remains quite good by fixing it at a value of -20 g/cm$^2$. The other parameter $\lambda$ is found to have a slow variation with energy and mass of the primary particle, with a central value of 70g/cm$^2$. We fix both at the values suggested here in our reconstruction procedure for real events. One of the benefits of fixing those relatively insensitive parameters is to reduces the chances of the parameter search being trapped at a local minimum of $\chi^2$.

Once the shower parameters are determined as a function of energy, the number of electrons can be calculated by using the G-H function (2) at depth $X$. The electrons are distributed laterally according to the NKG function at corresponding age $s$ of the shower.

The fluorescence and Cerenkov light and the corresponding signal appearing at the HiRes detector can then be generated.

### C. Muon Lateral Density and Arrival Time Distribution.

The simulation of muons in an EAS is much more complex. The dependence on both zenith angle and energy is important since the observation is done at a fixed altitude. In order to simulate the MIA trigger correctly, we generate the muon density, $\rho_\mu(R)$ at a distance $R$ to the core according to the muon lateral distribution. $\rho_\mu(R)$ and its fluctuation behavior are parameterized based on simulations. The muon density generated based on our parameterization is plotted in the FIG.7 a). As a comparison, the AGASA muon lateral density function(LDF)[3] and the Griesen LDF are plotted in the same figure. Our simulation agrees with the AGASA LDF well except in the small core distance area in which our simulation is closer to the Griesen function.

The arrival time of the EAS muon is essential in the simulation for MIA triggering. We parameterize the distribution of arrival time for each muon in the shower disk within different annular rings at a distance $R$ from the core, and at all zenith angles and energies in the grid mentioned above. The shape of the arrival time distribution changes quite rapidly with $R$ as can be seen in FIG. 7 c). Note the vertical scales are different for the different cases. We use a single function

$$\frac{dN}{dt} \propto t^{\alpha} \exp\left\{\frac{-t^{\beta}}{\tau}\right\}, \tag{5}$$

to describe all these distributions. The parameters $\alpha$, $\beta$ and $\tau$ are tabulated as functions of $R$, energy and zenith angle. The parameters are generated with due regard to correlations if they exist and the muon arrival time are generated individually depending on how many muons are generated at $R$ and for a specific direction. The median time for muons generated in an annular ring at $R$ reveals the curvature of the shower front. In figure b), we plot two examples at zenith angle $\theta = 0^\circ$ and $40^\circ$. The small differences between proton and iron induced showers are also shown in the figure. The lines represent the results directly from CORSIKA simulation and the dots are from our proton shower generator.

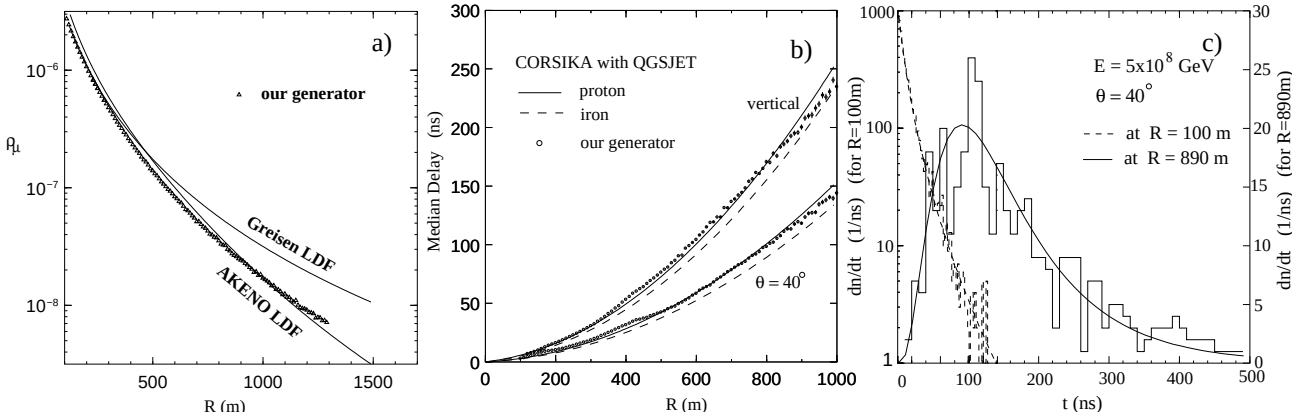


FIG. 7: Lateral distribution of $\mu$-density, shower $\mu$-front and time structure of $\mu$-disk at 870 g/cm$^2$

### D. Detector Response and Resolution

Once the shower is generated by the CORSIKA based driver, fluorescence and Cerenkov light contributions are calculated for each 0.04° angular bin along the axis of the shower. Cerenkov light generated in the previous bins is accumulated taking account of the attenuation between the bins due to the scattering of the light on atmospheric molecules and aerosols. The propagation and attenuation of light through the air and acceptance of the light by the detector are simulated in detail. The effective area and reflectivity of the mirror, filter transmission on the face of the focal plane camera, quantum efficiency of the PMT cathode, the gain of PMT and all electronics triggering and charge integration are realistically simulated. The variation of all these effects with wavelength is considered by tracking the light in 16 different UV wavelength bands covering from 300 to 400 nm. Finally, the simulated signal in each pixel is built up by summing all the angular bins involved and the 16 wavelength bands. The night sky background light is also added to the signal according to results of an on site measurement[22]. The trigger time slewing (i.e. late triggering for small pulses) is also taken into account for the HiRes sample-and-hold electronics.

The MIA signal is generated by sampling the number of muons for each counter at the perpendicular distance $R$ to the shower axis, then run over all muons in each counter to generate the arrival time for each of them. The pulse from a given counter is built up by passing all the muon signals through the electronics sequentially. Dead counters, counter efficiencies, trigger formation, time windows for accepting counter hits and noise muons are taken into account in the simulation. Both the HiRes and MIA signals are written in the

same format as for the real data.

8000 proton and 4000 iron induced showers are generated with a spectrum of trial energies from $5 \times 10^{16}$ to $5 \times 10^{18}$eV. The differential spectral index is set as -3.0. All the simulated events are passed through the same reconstruction procedure as real data and all geometrical and shower development parameters are determined. Events must pass the "quality cuts" defined below. We compare the overall distributions from the simulated events with data. This is plotted in FIG. 2,3,5. The solid(open) squares represent the showers induced by protons(iron nuclei) in those figures. The consistency between the data and simulation builds up our confidence in the simulation, and hence in the resolution functions we now present. Since we know the input parameters for every event, we can study the detector response and the corresponding resolution function on an event by event basis. In FIG. 8, the resolution functions in shower arrival direction, core location, energy and $X_{max}$ are plotted for iron induced showers. In a), we plot the distribution of the "opening angle" between the "real" shower axis vector given by the input shower and the "reconstructed" shower axis vector which is determined by using of the timing information from both HiRes and MIA. Similarly in b), we plot the distribution of the distance between the input shower core and the reconstructed core position. Those two geometrical resolution functions peak at zero but the long tails imply that some events are measured poorly.

We now move to a more quantitative discussion of parts c) and d) in the figure, the resolution functions in energy of primary particle and shower maximum depth, respectively. These are the most important results for the energy spectrum measurement and the composition study described in this paper.

### E. Hybrid "Good" Event Criteria versus Resolution

The better the geometrical parameters of a shower are determined, the better the shower development profile can be extracted. Of all geometrical parameters, the shower-detector-plane is the most crucial and depends strongly on how many tubes are triggered and how long the track formed by those tubes is. The number of muons detected by MIA is the other contributor to precise time fitting. In order to locate the shower maximum, it and a good fraction of the rest of the profile must bee seen by the detector. Moreover, as mentioned before, we must avoid those events which are dominated by Cerenkov light. Poorly fitted

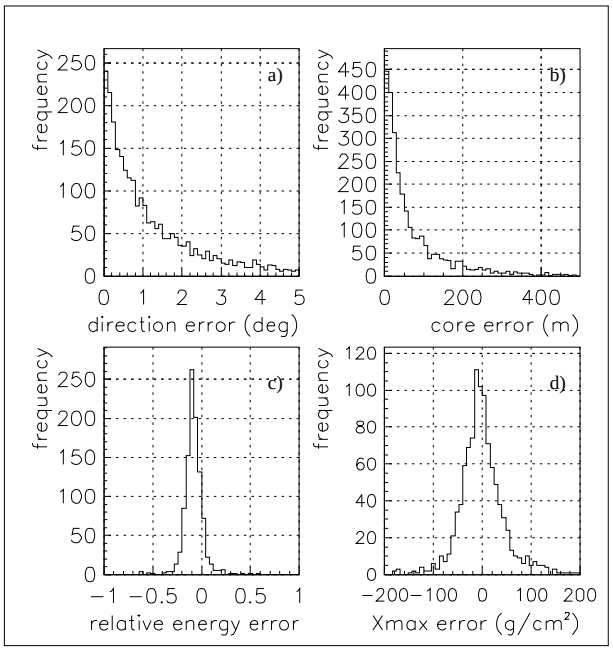


FIG. 8: Resolution functions of shower arrival direction a), core location b), shower total energy c) and depth of shower maximum d). The differences between the generated values of those variables in MC and those obtained from the reconstruction of the detector output are plotted here. Energy error is in $(E - E_{in})/E_{in}$ in c), where $E_{in}$ is the input from the simulation.

events should also be rejected. The set of quality cuts listed in Table. I addresses these issues. The first four criteria in this table are self explanatory while the fifth throws out events which come towards the detector and are dominated by Cerenkov light. This cut reduces the Cerenkov light contribution to less than 75% of the total amount of light in each event. The average Cerenkov light is about 25%. The last two cuts control the fitting quality.

After these tight cuts, the means and widths of the resolution functions, as shown in FIG. 8, are summarized in Table. II. The resolution is significantly improved compared with the Fly's Eye experiment. In that experiment the energy resolution was 33% (monocular) and 24% (stereo) below $2\times10^{18}$eV[23] and the $X_{max}$ resolution was 50 g/cm$^2$ averaged over a broader energy range up to $10^{19}$eV[2]. Most importantly, there is no bias observed in the present experiment with these cuts. The resolution functions show negligible systematic shifts except in energy. Those shifts go in opposite direction for proton and iron induced showers. This is discussed further in Sec. II F.

| Variables | cuts |
|---|---|
| Track Angular Length | $> 20^\circ$ |
| $R_{p_{MIA}}$ | <2 km |
| $X_m$ | $X_l < X_m < X_h$ |
| Spanning | $X_h - X_l > 250$ (g/cm$^2$) |
| $\theta_h$ | $> 10^\circ$ |
| $\Delta X_m$ | $< 50$(g/cm$^2$) |
| $\chi^2$ per DOF | <10 |

TABLE I: Event criteria. $X_h(X_l)$ refers to the depth of the highest(lowest) section of the shower track seen by the detector. $\Delta X_m$ is the estimated error in $X_{max}$.

| QGSJET | proton | | iron | |
|---|---|---|---|---|
| | $\sigma$ | mean | $\sigma$ | mean |
| E (%) | 16 | 8 | 10 | -13 |
| $X_{\max}$ (g/cm$^2$) | 44 | 7 | 44 | -2 |
| $X_{core}$ (m) | 42 | -2 | 40 | -1 |
| $Y_{core}$ (m) | 57 | -2 | 55 | 2 |
| space angle | 0.88° | | 0.83° | |

TABLE II: Resolution figures for a $E^{-3}$ differential spectrum seen by HiRes and MIA. Quality cuts have been applied. Space angle errors are median values.

The other important issue is the energy dependence of those resolution functions. Because of the constraint from MIA, all the well reconstructed showers are at a similar distance from the HiRes detector. The energy and $X_{max}$ variables, which are mainly determined by HiRes, thus have a resolution function which varies slowly with energy. They appear slightly worse at $10^{17}$eV due to closeness to the detector threshold. The width of energy resolution shown as FIG. 8 c) changes from 11% at $10^{17}eV$ to 6% at $10^{18}$ eV for iron induced showers. The $X_{max}$ resolution changes from 48 g/cm$^2$ to 41 g/cm$^2$ over the same range.

In summary, we have established the validity of our full Monte Carlo code for the HiRes/MIA detector and for the reconstruction procedure. We evaluate the resolutions for all interesting variables and optimize the resolution by selecting "good" events with a

set of tight cuts which do not cause bias. Under these criteria, 891 real events remain. They form the data base of our measurement of energy spectrum and investigation of composition of cosmic rays in the energy range covered by this data set.

## IV. PHYSICS RESULTS

We measure the cosmic ray intensity as a function of energy and study the cosmic ray composition in the energy range from $10^{17}$ to $3 \times 10^{18}$ eV using this experimental data set and the detailed Monte Carlo study. All the results are summarized in this section.

### A. Aperture Estimation

As shown in FIG. 5, the shower energy distribution peaks at $3 \times 10^{17}$ eV, which points to a fully efficient observation above $4 \times 10^{17}$ eV. The distribution falls off rapidly below $3 \times 10^{17}$ eV due to trigger inefficiency. In order to measure the cosmic ray energy spectrum, a correction for the detector aperture is necessary.

There are two ways to estimate the aperture of the hybrid detector. One way is to use the full simulation code, calculate the observation efficiency with the same reconstruction, and event selection criteria at several fixed energies in this energy region. The other way is to use the measured core location and arrival direction distributions of the observed events directly .

Above a certain energy, the hybrid detection scheme becomes fully efficient and the aperture should exhibit a plateau for events near the center of the detection volume and within a given solid angle. This indicates that the detector is fully efficient in this kernel of the detection volume. The hieight of the plateau provides a normaliztion reference for the distribution of detector efficiency as a function of solid angle and location within the detection volume. The detector aperture can be estimated by integrating this normalized efficiency distribution over the whole area and $2\pi$ solid angle. In our case, we find that this kernel corresponds to an area with 0.8 $km$ radius centered at MIA and a cone with 30° zenith angle. For a distribution of 182 events with energy higher than $10^{17.6}$ eV, the integral yields an aperture of about 5.2 $km^2 \cdot Sr$. By using this method, one can avoid the modeling dependence inherent in the MC simulation. However, poorer statistics will result a large

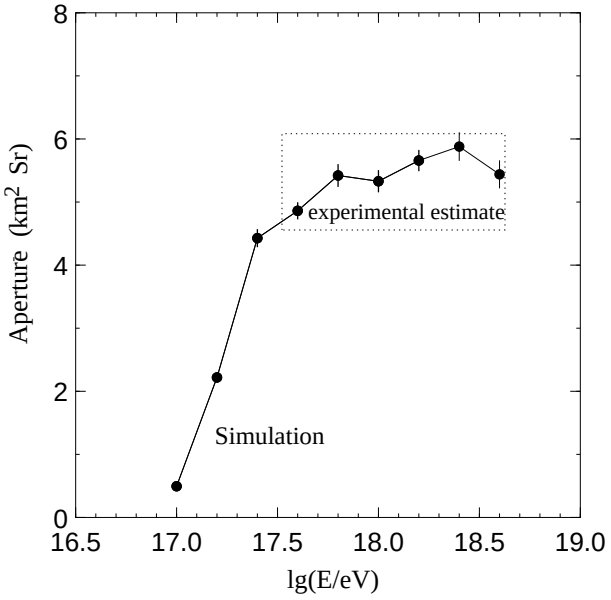


FIG. 9: The detector aperture as a function of primary energy. Dots connected by solid line represent the simulated result. The area marked by the doted line gives a range of the experimentally estimated aperture with its uncertainty.

uncertainty in the aperture. FIG. 9 shows the results. The area surrounded by the dotted line indicates this experimentally estimated aperture with an uncertainty of $0.8km^2 \cdot Sr$ dominated by statistic error.

The Monte Carlo method provides a more precise estimate. Every point in the figure represents about 3,000 events. Above $10^{17.6}$ eV, the calculation shows that the detection efficiency is saturated and this aperture is consistent with the experimental estimate. The feature of a flat aperture as a function of energy, provided by the MIA detector, is very useful for the cosmic ray intensity measurement. The price for this feature is that the aperture is rather small. The MC method provides a calculation of the aperture near detector threshold with good precision. The fluorescence detector has a sharp threshold around $10^{17}$ eV. Since the efficiency drops to lower than 10%, the events below this energy are not included.

### B. Energy Spectrum

FIG. 10 shows the cosmic ray energy spectrum from $10^{17}$ eV to $2.5 \times 10^{18}$ eV. The total exposure is about $1.45 \times 10^{13}\ m^2 \cdot Sr \cdot sec$. In order to see the detailed structure of the energy spectrum, the intensity is multiplied by $E^3$. Due to the small exposure, statistics are poor

| $\log_{10}$ (E/eV) | J(E) | $\Delta$ J |
|---|---|---|
| | $(10^{-28} \cdot eV^{-1} \cdot m^{-2} \cdot Sr^{-1} \cdot s^{-1})$ | $(10^{-28} \cdot eV^{-1} \cdot m^{-2} \cdot Sr^{-1} \cdot s^{-1})$ |
| 17.07 | 22.3 | 1.7 |
| 17.21 | 8.04 | 0.58 |
| 17.35 | 3.05 | 0.23 |
| 17.49 | 1.15 | 0.11 |
| 17.63 | 0.542 | 0.064 |
| 17.76 | 0.130 | 0.026 |
| 17.90 | 0.049 | 0.014 |
| 18.04 | 0.0244 | 0.0081 |
| 18.20 | 0.0054 | 0.0031 |
| 18.36 | 0.0012 | 0.0012 |
| 18.41 | 0.00105 | 0.00105 |

TABLE III: The cosmic ray energy spectrum from $10^{17}$ eV to $3 \times 10^{18}$ eV.

above $3 \times 10^{17}$ eV. Nevertheless, the data supports an overall power law spectrum with an index about -3.10 and a intensity of $10^{-29.45} eV^2 \cdot m^{-2} \cdot Sr^{-1} \cdot s^{-1}$ at $10^{18}$ eV. The data of this spectrum is listed in Table III.

As a comparison, the stereo Fly's Eye [2] measured energy spectrum is plotted in the same figure. The new measurement is consistent with this Fly's Eye result. The difference between the two measured intensities is less then 8% below $3 \times 10^{17}$ eV.

The new measurement marginally confirms the energy spectrum break occurring around $3 \times 10^{17}$ eV in the old Fly's Eye stereo data. This break is not seen in the Fly's Eye monocular data set because of poorer energy resolution. Since the HiRes/MIA experiment has even better energy resolution, it should see this break if it exists.

In order to avoid possible binning bias inherent with such low statistics, we plot the integrated energy spectrum in FIG. 11. The break in the spectrum is clear. By using a least $\chi^2$ fit, we find that the break occurs around $10^{17.5}$ eV. The spectrum parameters are summarized in the table. IV. The raw energy distribution is plotted in the same figure to demonstrate the effect of the detector aperture correction. Above $10^{17.6}$ eV where the aperture is flat, the absolute value of the spectrum index is too large to be consistent with

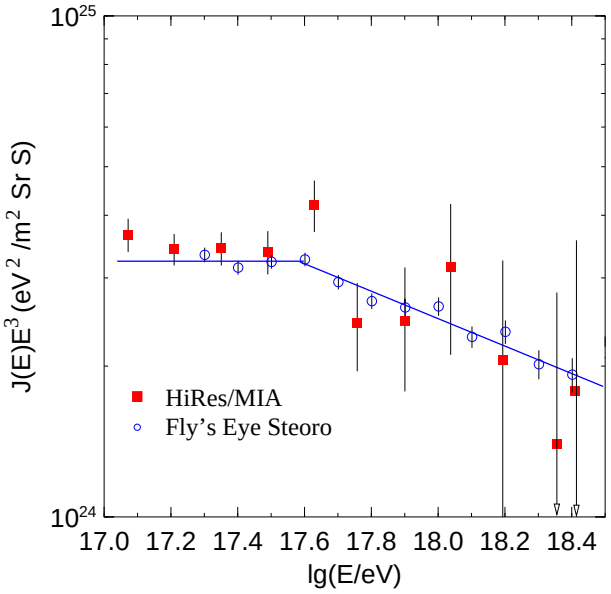


FIG. 10: The differential energy spectrum of cosmic rays in the vicinity of $3 \times 10^{17}$ eV. $E^3$ is multiplied to the intensity. The result from this experiment (squares) is consistent with the Fly's Eye experiment (dots). The lines represent the fit according to Fly's Eye data[2].

| Energy (eV) | Index | lg(J($10^{18}$ eV)) |
|---|---|---|
| $10^{17.0} \sim 10^{17.5}$ | $-3.07 \pm 0.11$ | -29.45 |
| $10^{17.5} \sim 10^{18.4}$ | $-3.52 \pm 0.19$ | -29.55 |

TABLE IV: The parameters of cosmic ray energy spectrum. Both components are listed with their energy range. The normalization of the cosmic ray intensity, J, is provided at $10^{18}$ eV for both cases, in $m^{-2} \cdot Sr^{-1} \cdot s^{-1} \cdot eV^{-1}$.

the lower energy measurements [1]. The energy spectrum below $10^{17.3}$ eV requires a large correction but it is significantly different from the power law fit to the correction-free data above $10^{17.6}$ eV and in good agreement with lower energy experiments.

### C. Resolvability of Composition: $X_{max}$ and $E.R.$

As mentioned in the introduction, the distribution of $X_{max}$ can be used with the help of Monte Carlo simulations to extract an average composition of primary cosmic rays. The results depend on the hadronic interaction model, the EAS simulation model and resolution

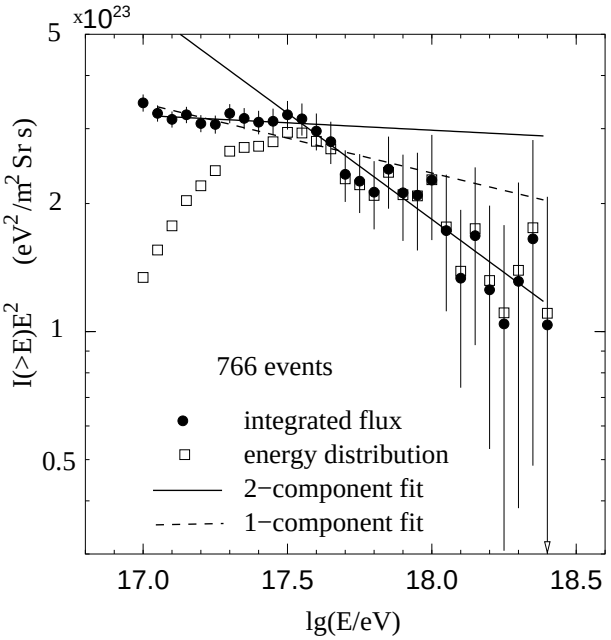


FIG. 11: The integrated energy spectrum of cosmic rays measured with this experiment (dots). $E^3$ is multiplied to the intensity. Open squares show the energy distribution before the aperture correction. Solid lines represent a fit of power law with two indices and dashed line shows an overall fit.

of the detector in energy and $X_{max}$. In this paper, we compare data to the predictions of two hadronic models: QGSJET and SIBYLL. Other, lower multiplicity models have been shown to be inconsistent with any normal composition of cosmic rays.

According to the simulation, the average $X_{max}$ for showers induced by protons is separated from the average for iron by about 100 g/cm$^2$ and this separation is almost independent of energy in the range from $10^{17}$eV to $10^{18}$eV. Since the resolution of the detector is 44g/cm$^2$, we can tell if the data is closer to one than the other. The absolute position of $\overline{X_{max}}$ for a given composition assumption is model dependent (about 25 g/cm$^2$ shift). At any given energy, a measurement of $\overline{X_{max}}$ implies a particular composition which is thus systematically uncertain. On the other hand, an apparent departure of the data points from either of the predictions based on proton or iron showers as a function of energy will reveal information on the change in the composition of cosmic rays. The rate of this change can be much more reliably determined than the absolute composition itself.

The variation of the separation between the measured and simulated pure composition $X_{max}$ can be quantitatively evaluated using the so called "elongation rate". Based on models,

it is found that the average $X_{max}$ increases with energy logarithmically over the energy range of interest. The "elongation rate" is symbolized by $\alpha$ in this paper and defined by

$$\overline{X_{max}} \propto \alpha \log E. \tag{6}$$

It is remarkable that the elongation rates are almost the same for proton and iron induced showers and nearly independent of the interaction models. They are $58.5 \pm 1.3 \mathrm{g/cm^2}$ per decade of energy for proton showers and $60.9 \pm 1.1 \mathrm{g/cm^2}$ per decade of energy for iron showers according to the QGSJET model. Any other values for E.R. observed from the data will indicate a change in composition.

An important issue associated with measuring the elongation rate is possible existence of a bias caused by tight cuts. To test this, we compare the average $X_{max}$ as a function of energy using the simulated events. One set of data is based on all the CORSIKA sampled events and the other is based only on those that trigger the detector, are able to be reconstructed and pass the tight cut criteria. As shown in FIG. 12, no matter what interaction model is used, we do not see any bias using the cuts set in the Table. I. The thin lines in the figure show the sampled events and the circles and the squares show the reconstructed results (see the figure legends for details).

### D. The Change of Cosmic Ray Composition

The HiRes/MIA experimental data as shown in the FIG. 12 demonstrates an unambiguous change in average $X_{max}$ with energy. This indicates a change towards a lighter mix of nuclei in the average composition from $10^{17}$ to $10^{18}$eV. This indication of change in composition can be evaluated by using the elongate rate measured in the experiment, i.e.

$$\alpha = 93.0 \pm 8.5 \pm (10.5) \qquad (\mathrm{g/cm^2}), \tag{7}$$

where the number in parentheses represents the systematic error discussed below. In comparison with the predicted number for a unchanging or pure composition mentioned above, the difference is larger than any known uncertainties. The uncertainty in predicted elongation rate due to hadronic model dependence is small.

We can estimate the change of the composition in the form of the average logarithm of atomic number of the primary nuclei, $\Delta\overline{lnA}$, as $-1.5 \pm 0.6$ over the energy range covered by

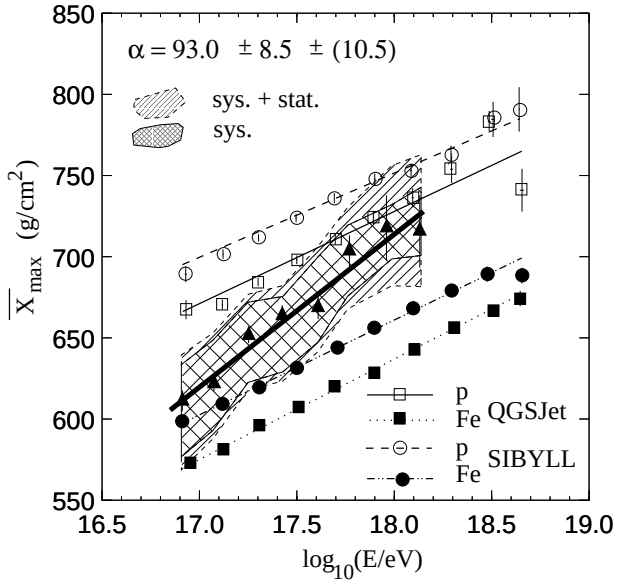


FIG. 12: Average $X_{max}$ increasing with energy. Shaded areas and the thick line within the area represent HiRes data and the best fit of the data respectively. The closed triangles represent the data set corresponding to the central values of the parameters in the reconstruction. The circles, squares and lines refer to the simulation results. See text for details.

the data. This number is quite model independent assuming equal elongation rate for all different pure compositions. The systematic uncertainty in $\alpha$ is included here. The absolute value of $\overline{lnA}$ is strongly model dependent as implied by FIG. 12.

### E. Uncertainties in $X_{max}$ and Energy

Uncertainties in $X_{max}$ come both from choice of theoretical models and detector resolution. We first look into the uncertainty in the predictions. In FIG. 12, the average difference in $X_{max}$ at any given energy between the predictions based on QGSJET and SIBYLL models is about 25g/cm$^2$. Both are compatible with the data and both lead to the same qualitative conclusion of a lightening in the composition. However, the value of the average $lnA$ at any given energy is model dependent.

From the experimental point view, we have made a detailed effort to understand the systematic error in shower $X_{max}$ and energy. For $X_{max}$, we have considered systematic errors in the atmospheric transmission of light and in the production of Cerenkov light. These are related since scattered Cerenkov light can masquerade as fluorescence light if not accounted

for properly. For atmospheric scattering, there is uncertainty in the aerosol concentration and its vertical distribution. The uncertainty, equivalent to one standard deviation with respect to the mean, is expressed as a range of possible horizontal extinction lengths for aerosol scattering at 350 nm (taken as 11 km to 17 km based on measurements using Xenon flashers, [17]) and a range of scale heights for the vertical distribution of aerosol density above the mixing layer (taken as 0.6 km to 1.8 km). For Cerenkov light production, we have varied the angular scale for the Cerenkov emission angle over a one standard deviation equivalent. At ground level, we take the distribution as an exponential function of the angle from the shower axis, with a scale of $4.0 \pm 0.3^{\circ}$[1]. Those uncertainties are shown by the shaded area in FIG. 12.

The systematic error in the energy is about 25% and comes from fluorescence efficiency uncertainty[6], detector calibration uncertainty[24] and the atmospheric corrections[23]. The first two are intrinsically independent of the primary particle energy over this range. The fluorescence efficiency has been measured with an error of 10%. The percentage atmospheric corrections are also independent of energy because the sample of showers is restricted to core locations within 2 km of the MIA detector center. Therefore there is no significant atmospheric path length difference between an EAS and the detector for different energies. An energy independent systematic fractional error in energy has no effect on the measured elongation rate. The magnitude of the systematic error in energy due to atmospheric attenuation can be estimated by varying the atmospheric parameters over the range described above. It is not greater than 10%. The detector calibration systematics is less than 5%.

### F. $X_{max}$ Distribution

In FIG. 6, we can see that the fluctuations about the average $X_{max}$ for simulated proton showers is larger than that for iron showers. The fluctuations for both proton and iron induced showers are too large to allow us to distinguish one from the other on an event by event basis. However, we can determine the gross properties of the composition statistically. In FIG. 13 we plot the predicted distributions of $X_{max}$ for proton and iron showers together with dotted and dashed lines, respectively. The detector response has been folded into those distributions. By studying those distributions in different energy ranges as shown in the figure, one can compare the data to pure proton and pure iron composition distributions.

The data clearly requires a mixed composition of light and heavy particles to account for the width and peak value of the $X_{max}$ distribution.

### G. Comparison with Previous Experiments

The cosmic ray energy spectrum measured by all modern experiments are summarized in the FIG.14 covering the whole energy range from $3 \times 10^{14}$ to $3 \times 10^{18}$ eV. The consistency between this experiment and the Fly's Eye stereo data has been discussed previously. We have shown the marginal confirmation of the break in the spectrum at $3 \times 10^{17}$ eV there. By comparing with the observations [25] in the "knee" region, we see that both the intensity and spectrum index imply a good continuity from the results at energy lower than $3 \times 10^{16}$ eV. We especially note that the change in cosmic ray intensity around $3 \times 10^{17}$ eV is comparable in power law index with the change that occurs around the "knee". A confirmation of this break with better statistics and similar energy resolution is important. All the other experimental results are consistent with the Akeno result: the spectrum follows a single index power law between $10^{16}$ and $10^{17}$ eV.

The only existing experimental result based on direct measurements of shower longitudinal development is that from Fly's Eye experiment. As a successor of that experiment, the HiRes/MIA experimental result qualitatively supports old Fly's Eye's result, i.e. there exists a trend in the composition of cosmic rays to a lighter mix with energy. Quantitatively, they are consistent with each other, taking into account the systematic errors in the original Fly's Eye result of about 25 gm/cm$^2$ on individual $X_{max}$ measurements. The elongation rate measured in HiRes/MIA experiment is marginally larger than that in Fly's Eye[23] which is $78.9 \pm 3.0\,\mathrm{g/cm^2}$/decade where the quoted error is statistical only. We should also note that experimentally measured elongation rates are not corrected for acceptance. Differences in acceptance for two experiments could introduce differences in elongation rates. The safest method is to compare each experiment to its own simulated proton and iron data sets. The conclusion on the composition of cosmic rays based on this kind of comparison is meaningful because the detector effects are counted in exactly the same way for both real and simulated events. For the present experiment, based on our simulation, we believe that the detector biases for the elongation rate are minimal. In summary, when all the errors are taken into account, the results on $X_{max}$ distribution and elongation rates, from the two experiments

are consistent, in spite of the differences in the analysis.

The other existing result on elongation rate in the same energy range is from the Yakutsk experiment[26]. The systematic error is not provided and the method using a ground array experiment is more indirect than the present experiment. Nevertheless, the results are marginally in agreement with the result reported here.

There are several measurements of elongation rate at lower energies, between $10^{14}$ and few $10^{16}$ eV. These results and ours are shown in FIG. 15 together. The trend of a changing cosmic ray composition shows a pattern correlated with breaks in the energy spectrum. It can be characterized qualitatively as follows. There is a rather clear break around $3 \times 10^{15}$ eV which is related to the "knee" in the energy spectrum. This break seems to be confirmed by several experiments [1]. The elongation rate shows an increasingly heavy composition around this knee. Above $3 \times 10^{17}$ eV, the composition changes to a lighter mix. It seems to be correlated to the spectral break observed by Fly's Eye experiment which is marginally confirmed by this experiment. Those experiments imply a relatively unchanging region between $10^{16}$ and $10^{17}$ eV but no measurements of elongation rate exist between $10^{16.4}$ and $10^{17}$ eV.

## V. CONCLUSION

The HiRes/MIA hybrid experiment has measured the cosmic ray energy spectrum between $10^{17}$ and $3 \times 10^{18}$. The spectral index and intensity are given in Table. IV. The result is in agreement with the Fly's Eye experiment. This result marginally supports the Fly's Eye stereo observation of a break in the energy spectrum at $4 \times 10^{17}$ eV.

The HiRes/MIA hybrid experiment confirms the Fly's Eye experimental result that the elongation rate is different from simulation with an unchanging composition. Modern hadronic interaction models and improved detector resolution in energy and $X_{max}$ do not change the original conclusion. Within errors, the elongation rate observed in this experiment, $93.0 \pm 8.5 \pm (10.5)\,\mathrm{g/cm^2/decade}$, is consistent with previous experiments, such as Fly's Eye and Yakutsk[26]. While the conclusion regarding the absolute value of $\overline{lnA}$ of the primary composition depends on the interaction model used, this study shows that the elongation rate is stable with respect to choice of models. In the light of this, the amount of the change in the average composition, i.e. $\Delta\overline{lnA} = -1.5 \pm 0.6$, is largely model independent,

no matter what value of $\overline{lnA}$ the change starts from.

Putting all experimental results together from $3 \times 10^{14}$ to $3 \times 10^{18}$ eV, we note that there seems to be a correlated patterns in the energy spectrum and elongation rate, $X_{max}$ vs. energy, plot. Both measurements in energy spectrum and $X_{max}$ imply a continuity from lower to higher energies, with a flat bridge between $10^{16}$ and $10^{17}$ eV.

We note that following the break, the Fly's Eye experiment [2] reports a hardening of the spectrum near $5 \times 10^{18}$ eV. This has been interpreted as evidence for the emergence of an extragalactic component above a softer galactic component [2]. A change from a heavy to a light composition in this energy region also gives support to a changing origin for those cosmic rays. The lack of a strong galactic anisotropy at the highest energies would also rule out galactic sources for energetic protons [27]. A number of new experiments, such as HiRes, the Pierre Auger Project, the Telescope Array, EUSO and OWL will address this issue.

## VI. ACKNOWLEDGEMENTS

We acknowledge the assistance of the command and staff of Dugway Proving Ground. This work is supported by the National Science Foundation under contract No. PHY-93-21949, PHY-93-22298 and U.S. Department of Energy and the Australia Research Council.

---

[1] L. F. Fortson *et al., Proceedings of the 26th International conference (ICRC), Salt Lake City, 1999*, edited by D.Kieda *et al.*,(Univ. of Utah, Salt Lake City,1999),Vol.3, p.125; K. H. Kampert *et al.*, *ibid.*, Vol.3, p.159; F. Arqueros *et al.*, astro-ph/9908202; M.A.K. Glasmacher *et al.*, Astropart. Phys. **12**, 1, (1999).

[2] D. J. Bird *et al.*, Phys. Rev. Lett. **71**, 3401, (1993).

[3] N. Hayashida *et al.*, J. Phys. **G 21**, 1101, (1995).

[4] B. R. Dawson, R. Meyhandan and K. M. Simpson, Astropart. Phys. **9**, 331, (1998).

[5] T.Abu-Zayyad *et al.*, Phys. Rev. Lett. **84**,4276,(2000).

[6] T.Abu-Zayyad *et al.*, "The Prototype High Resolution Fly's Eye Cosmic Ray Detector", to be published in Nucl. Instrum. Methods **A**.

[7] T. Gaisser and A. M. Hillas, *Proceedings of the 15th International conference, Plovdiv, 1977*, (Bulgarian Academy of Sciences, Plovdiv, Bulgaria, 1977), Vol.8, p.353.

[8] R. M. Baltrusaitis *et al.*, Nucl. Instrum. Methods **A240** 410 (1985); R. M. Baltrusaitis *et al.*, *et al., Proceedings of the 19th International conference, La Jolla, 1985*, (NASA, Washington D.C.,1985) Vol.7, p.159

[9] A. Borione *et al.*, Nucl. Instrum. Meth. **A 346**, 329 (1994).

[10] K. D. Green, in "High Energy Gamma Ray Astronomy", AIP Conf. Proc., 220, 184 (1990).

[11] D. J. Bird *et al.*,"CASA-MIA-HIRES: A Hybrid Detector For Measuring Multiple Properties of $10^{17}$ eV Extensive Airshowers", submitted to Nucl. Instrum. Methods **A** (1999).

[12] F. Kakimoto *et al.*, Nucl. Instrum. Meth. **A 372**, 527 (1996).

[13] D. Heck *et al., preprint of Institut fur Kernphys., Univ. of Karlsruhe*, FZKA-6019, Feb., 1998 (Kernforschungszentrum, Karlsruhe, 1998).

[14] C. Song *et al.*, Astropart. Phys. **14**, 7, (2000).

[15] J. A. Richards and L. W. Nordheim, Phys. Rev. **74** 1106, (1948).

[16] M. Hillas, J. Phys. **G: 8**, 1461, (1982).

[17] T.Abu-Zayyad *et al., , Proceedings of the 25th International conference, Durban, 1997*,(Potchefstroomse Univ., Potchefstroomse, 1997), Vol. 5, p. 345.

[18] T. Abu-Zayyad *et al.*, "A Measurement of Longitudinal Development of the Cosmic Ray Air Shower Between $10^{17}$ and $10^{18}$eV", to be published in Astroparticle Phys., astro-ph/0008206.

[19] A. F. Bielajew, "Photon Monte Carlo Simulation", Report PIRS-0393, National Research Council of Canada (1993); A. F. Bielajew and D. W. O. Rogers, "Electron Monte Carlo Simulation", Report PIRS-0394, National Research Council of Canada (1993).

[20] N. N. Kalmykov, S. S. Ostapchenko & A. I. Pavlov, Nucl. Phys. **B52** (Proc. Suppl.) 17 (1997).

[21] R. S. Fletcher *et al.*, Phys. Rev. **D50**, 5710, (1994).

[22] J.W.Elbert,*Proc. Tokyo Workshop on Techniques for the Extremely High Energy Cosmic Rays, Tokyo, Japan, 1993*, edited by M. Nagano, (Institute of Cosmic Ray Research, Tokyo, 1993) p. 232.

[23] D. J. Bird *et al.*,Astrophys.**J 424**, 491, (1994).

[24] T. Abu-Zayyad *et al., Proceedings of the 26th ICRC(Ref.[1])*, Vol.5, p.429.

[25] M. Nagano *et al.* , J. Phys. G.**10**, 1295, (1984); J.W.Fowler *et al.*, astro-ph/0003190; M.A.K.Glasmacher *et al.*, Astroparticle Phys. **10**, 291, (1999); S.P.Swordy and D.B.Kieda,

astro-ph/9909381; M.Amenomori *et al.*, Astrophys. J., **461**, 408, (1996).

[26] Afanasiev B.N.*et al., Proc. Tokyo Workshop on Techniques for the Extremely High Energy Cosmic Rays, Tokyo, Japan, 1993*, edited by M. Nagano, (Institute of Cosmic Ray Research, Tokyo, 1993) p. 35.

[27] D.J. Bird et al., Ap.J. **511**, 739, (1999).

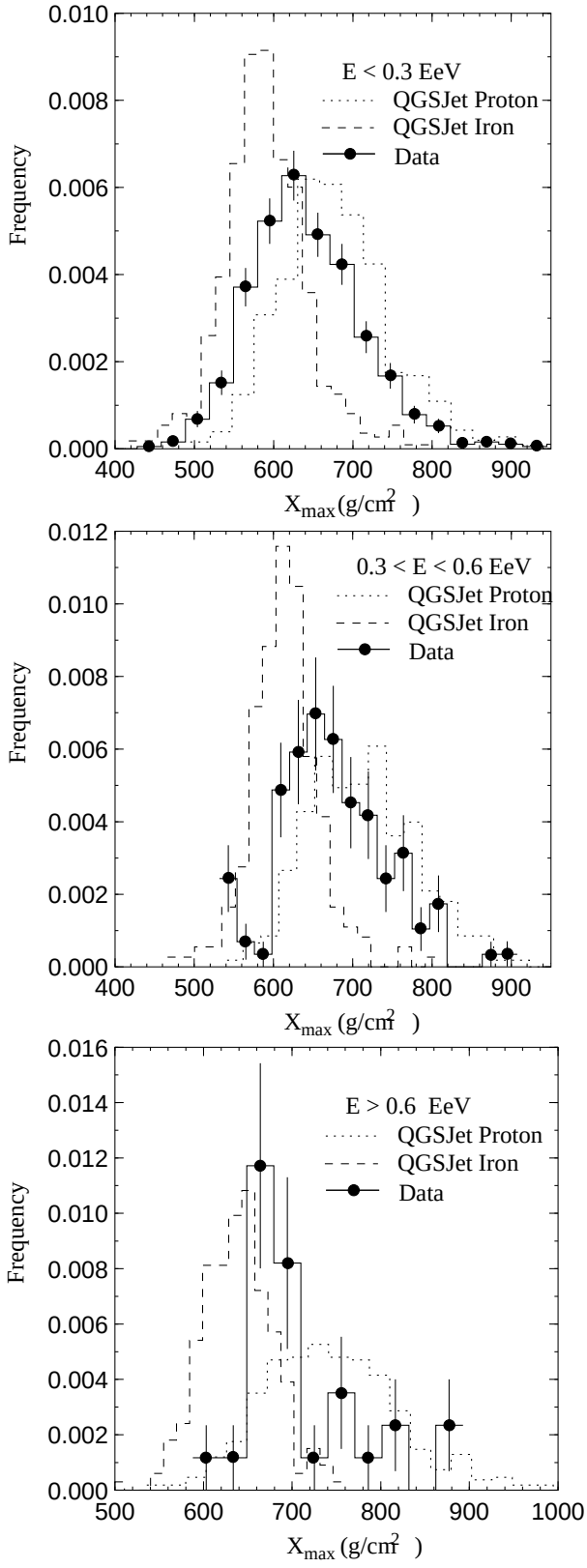


FIG. 13: $X_{max}$ distributions. Data from this experiment and simulated are compared. All distributions are normalized.

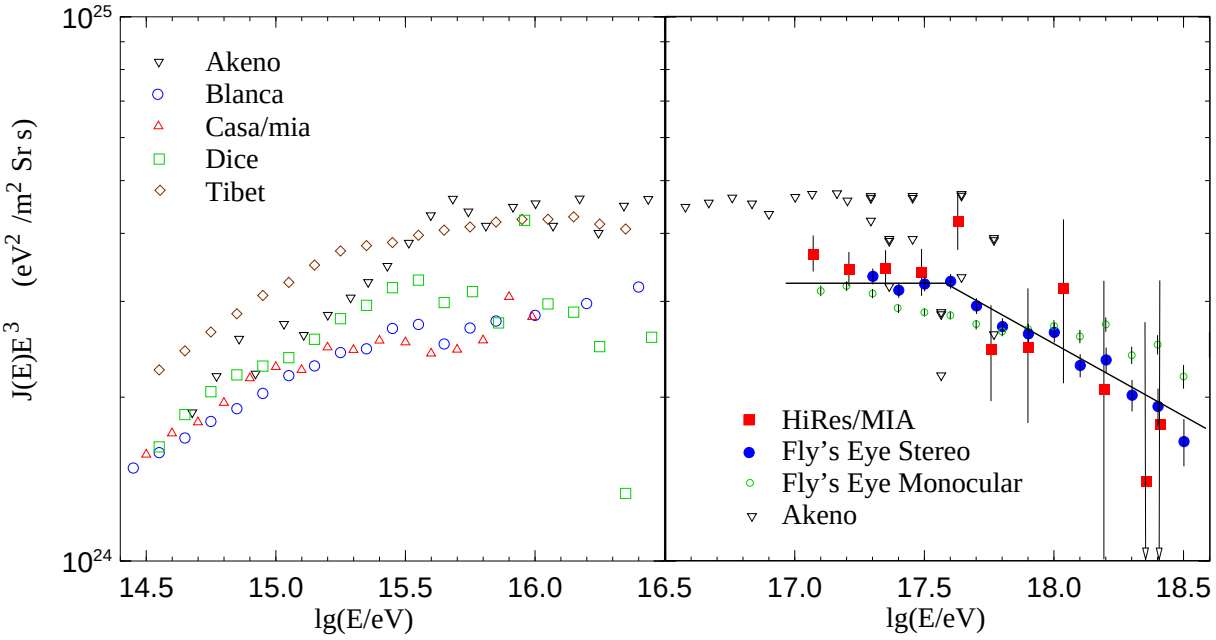


FIG. 14: Energy spectrum of cosmic rays from $10^{14.5}$ to $10^{18}$ eV. $E^3$ is multiplied to the intensity. Data in the vicinity of $3 \times 10^{15}$ eV are adopted from [1] (Blanca paper).

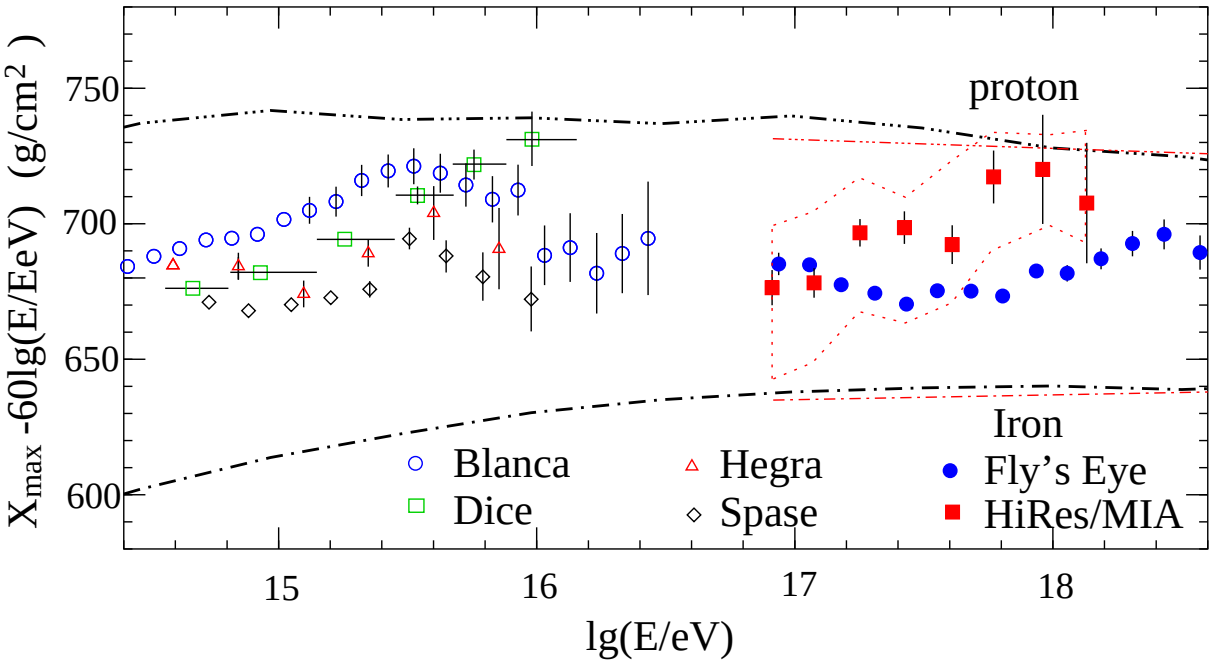


FIG. 15: Average depth of shower maximum as a function of primary energy of cosmic rays. An arbitrary elongation rate of 60 g/cm$^2$ is subtracted. Again, the data in the lower energy region is adopted from [1] (Blanca paper). Dashed lines with single-dots represent the simulated result from proton showers and dashed lines with three-dots for the iron showers. The thick lines are from [1] and the thin lines from this experiment.